Explosive-pusher-type laser compression experiments with neon-filled microballoons

B. Yaakobi, D. Steel,* E. Thorsos, A. Hauer, B. Perry, S. Skupsky, J. Geiger,† C. M. Lee, S. Letzring, J. Rizzo,
T. Mukaiyama,‡ E. Lazarus, G. Halpern,§ H. Deckman,§ J. Delettrez, J. Soures, and R. McCrory

Laboratory for Laser Energetics, University of Rochester, 250 East River Road, Rochester, New York 14623

Laser-irradiated targets filled with pure neon have been used to directly measure the peak density ρ and ρR product (density $\times$ radius) using spectrally and spatially resolved neon x-ray line emission. In agreement with theoretical predictions for the explosive-pusher mode, we find peak densities in the range 0.25–0.5 g/cm^3 which are almost independent of laser power or fill pressure. In addition, ρR values increase from 2×10^{-4} to 6×10^{-4} g/cm^2 as the fill pressure increases from 2 to 56 atm. Using these methods for the density measurement as well as other experimental signatures (such as x-ray pinhole imaging, x-ray streak photography, and x-ray line emission from the glass microballoon), we systematically investigated the explosive-pusher mode of target dynamics for various fill pressures. These and similar methods may become crucial in diagnosing future higher-compression implosions.

I. INTRODUCTION

Analysis of spectrally and spatially resolved x-ray emission from neon-filled glass micro-balloons is shown to be a powerful method for obtaining direct information on target implosion and compression. Even though the core of laser-fusion targets contains a thermonuclear fuel (deuterium-tritium mixture), the use of neon was thought to be beneficial in more than one way. First, a pure-neon-filled target, although not producing thermonuclear reactions, provides x-ray emission for compression studies[1] and normalization of hydrodynamic numerical codes. Second, one may add a small amount of neon for diagnostic purposes to an otherwise deuterium-tritium-filled target.[2] Finally, introducing neon actually modifies the behavior and performance of fusion targets and thus gives additional control of the process. These modifications are possibly of two kinds; if the neon quantity is sufficiently small it will not have a significant effect on the fill gas energetics but will inhibit heat conduction losses to the surrounding tamper.[3] This will prolong and enhance the thermonuclear-reaction process. When the amount of neon is increased, energy losses (due to both ion heating and excitation) dominate, and fill-gas cooling results. This cooling makes it easier to further compress the target.

The importance of neon-filled target experiments is best appreciated against the backdrop of present directions and limitations of laser-fusion experiments. First, x-ray neon spectra provide a direct measurement of the compression. Slowing down of α particles in the core is an additional method which, however, can be applied only at much higher compression values than those achieved in present-day experiments. Another

method which has been used for measuring compression is pinhole or zone-plate imaging of α particles[4]; however, these techniques only measure the diameter of the hottest region in the fuel and the relative error in the deduced compression is large (since compression depends on the cube of the measured core radius). Furthermore, the main thrust of laser-fusion experiments in the near future will most probably be to increase the compression (or, more precisely, the product ρR of density and radius) even at a loss of temperature. In such a case the diagnostic methods based on nuclear-reaction products may become ineffective but the pertinent x-ray emission of neon will still be useful down to a temperature near 200 eV. At still higher compression, neon lines would broaden to the point of being of marginal usefulness for diagnosis; however, lines from higher-Z ions may then be appropriate substitutes.

The present set of experiments was carried out in the explosive-pusher mode.[5] This means that the glass shell is exploded by suprathermal electrons (of long mean free path), which deposit their energy throughout the glass shell. Considerable effort has been devoted in this laboratory to the development of a detailed model for fast electrons which has been incorporated into a hydrodynamic code, LILAC.[6] Also, a semiempirical model[7] has been developed to predict the performance of explosive-pusher targets. The experimental results available for verifying these theoretical approaches have been mainly neutron yield, ion temperature (as inferred from nuclear reaction products time of flight), implosion velocity (from x-ray streak camera), and compression ratio (from x rays or α-particle imaging). We employ here some of these experimental methods but add spectroscopic methods of measuring the com-

pressed fill properties. This greatly enhances our ability to match theoretical predictions to the experiment. The difference between neon fill and deuterium-tritium (DT) fill is a modest rise in density and a decrease in ion temperature in the former case. However, for non-explosive-pusher-type experiments the effect of neon in increasing the peak compression is expected to be stronger.

The experiments reported here were extensively simulated by a one-dimensional hydrodynamic code LILAC, which includes a combination of diffusion and free streaming treatments of the suprathermal electrons and radiation transport of spectral line radiation. The following experimental parameters were calculated and compared with the experiment: density and temperature at peak compression, compression velocity, absolute intensity of x-ray lines, and total (filtered) x-ray intensity from the core and detailed x-ray spectral line shapes. The results of such calculations agree fairly well with the measurements. They improve our understanding of the compression dynamics and substantiate the results of the analysis described here.

II. EXPERIMENTAL ARRANGEMENT AND TYPICAL RESULTS

The laser used in these experiments was a four-beam silicate glass-rod system configured for target illumination in a plane. The nominal operating power was 160 GW in a pulse width between 40 and 80 psec with a repetition rate of 2 shots ph. The Nd:YAG oscillator was both actively and passively mode locked, with a contrast ratio of 10^6:1. The system output had a nearly uniform spatial intensity distribution at the last amplifier with a slowly varying transverse amplitude modulation (modulation depth ~50%). The four-beams
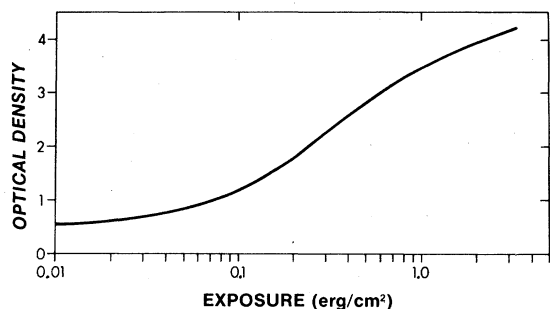
were focused with $f/2$ focusing lenses with 80% of the energy in a 60-μm-diam spot. (A more complete description of the system is given in Ref. 1.) Nominal target dimensions were 65-μm diameter and 0.6-μm wall thickness.

The absorbed laser energy was determined by measuring the energy of the blowoff plasma and x rays. This was accomplished by measuring the difference between a scattered light plus absorbed energy signal and only a scattered light signal in six two-channel pyroelectric calorimeters. The typical absorbed energy was close to 35%. Since this measurement was not a true 4π measurement, there is considerable uncertainty in this number.

Time-integrated plasma x-ray emission was diagnosed using crystal spectrographs and a pinhole camera for spectral and spatial information. The x-ray pinhole camera was a single-view, four-exposure, 12.5× magnification device. For every laser shot four pinhole exposures were taken using the following foil filtration: 25-μm-thick Be, 50-μm-thick Be, 75-μm-thick Be, and 50-μm-thick Be + 7-μm Al. The pinholes were 5 μm in diameter, electromachined in 12.5-μm-
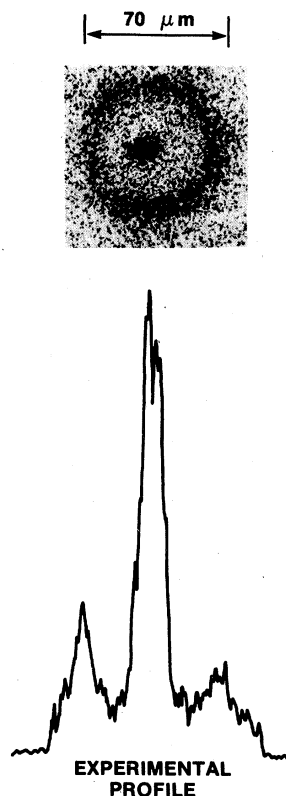
FIG. 2. Typical x-ray pinhole exposure and densitometer trace of a neon-filled target.

FIG. 1. Optical density of Kodak No-Screen film vs exposure for silicon K_α radiation.
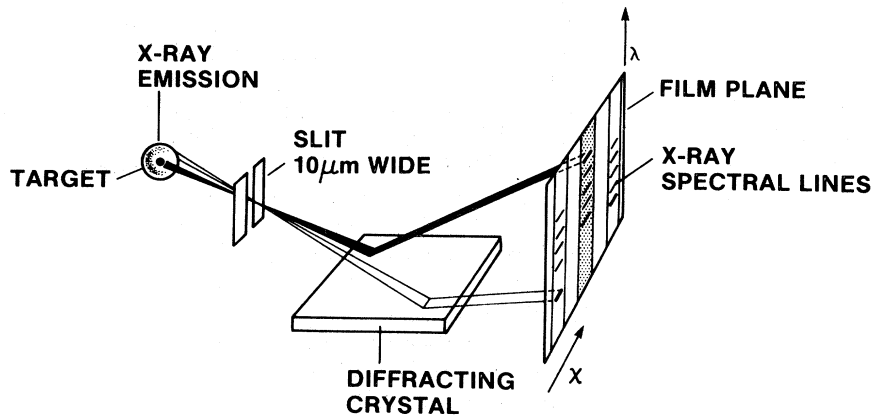
FIG. 3. Configuration for obtaining spatially resolved x-ray spectra.

thick nickel foil. The pinhole camera was located 45° out of the plane of illumination and was centrally located between two of the beams.

Kodak No-Screen film was absolutely calibrated for x-ray wavelengths in the range of interest. A fluorescent x-ray source with the targets Al, Si, and P was used. Fluorescent K_α radiation from these targets was collimated and then diffracted by a crystal before striking the film. The photon count rate was monitored with a flow proportional counter. An example of the calibration curves obtained by this method is shown in Fig. 1, and an example of a pinhole densitometer trace in Fig. 2.

Two spatially resolving crystal spectrographs were used in these experiments. Typically, one spectrometer would monitor the spectral range from 4–8 Å (silicon lines), while the other

covered the range 10–14 Å (neon lines). A thallium acid phathalate (TAP) crystal was used. The spectral resolution was determined by two factors: crystal broadening (finite angular acceptance for monochromatic radiation) and broadening due to the finite spatial extent of the source. Crystal broadening is usually determined by measuring the double-crystal rocking curves. Measurements have been made on TAP,[8] which indicate that its inherent broadening (at about 10 Å) is of the order of 3×10^{-4} rad. Differentiating Bragg's law we obtain $\Delta\lambda/\lambda = \Delta\theta/\tan\theta$. For $\lambda = 10$ Å the Bragg angle is $\theta_B = 22.7°$ (the $2d$ spacing of TAP is 25.9 Å). Thus for TAP the natural crystal broadening has a value for $\Delta\lambda/\lambda$ of 7×10^{-4} or $\Delta E \sim 0.9$ eV. The finite spatial extent of the radiating plasma also contributes to
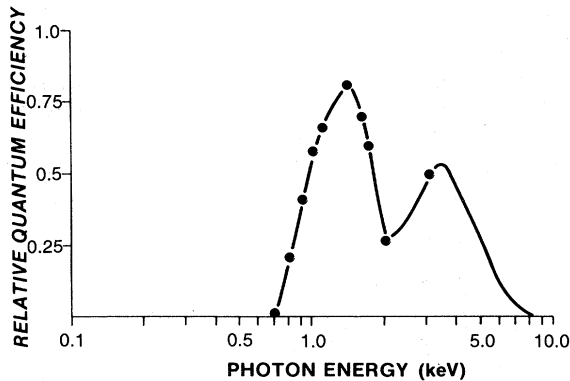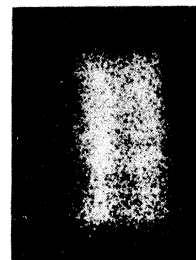

FIG. 4. Relative quantum efficiency of 78-Å-thick gold photocathode on 7-μm Be substrate with an additional 7-μm Be filter.

TIME ⟶   ⊢⊣
30 psec

FIG. 5. Time resolved x-ray emission of implosion from shot No. 17738.

spectral broadening. In the present experiments the target was typically located 20 cm from the film plane. Radiation from the glass shell (diameter ~6.0×10^{-3} cm) can thus have an angular spread of 3×10^{-4} rad or quite close to the spread caused by crystal broadening. Radiation coming from the compressed core would have a much smaller angular spread. In calculating the total instrumental broadening the two factors (due to the crystal and finite source size) are added in quadrature. For radiation coming from the compressed core it can be concluded that instrumental broadening is about 1.5 eV. All spectral information was recorded on Kodak 2491 or 2497 film (identical emulsions). Absolute calibration for this film is available in the literature.[9]

One-dimensional spatial resolution is provided by the slit shown in Fig. 3. The limitations on spatial resolution are the same as those encountered in the pinhole camera. Experimentally it was found that the minimum practical slit width was about 10 μm due to x-ray flux limitations.

A measurement of the hydrodynamic collapse time using an x-ray streak camera is important to allow a more complete comparison between experiment and hydrosimulation. On occasion, a slit was placed in front of the camera to provide spatially resolved information as well. The x-ray streak camera mounted directly on the experimental target chamber and shared a common vacuum with the chamber. In this way it was possible to use very thin filters (or no filters at all) since no vacuum window was required. The photocathode was a 78-Å-thick gold film, vacuum-deposited on a 7-μm Be substrate. In direct con-

tact with this substrate on the side facing the incoming flux was a 250-μm-thick disk of silver with a 100-μm-wide by 1-cm-long slit etched through it. This slit formed the entrance aperture and the temporally resolving slit for the camera. An additional 7-μm-thick Be foil served as an additional filter and to keep the plasma blow-off from entering the camera. The composite of filters and photocathode has a calculated quantum efficiency as a function of incident photon energy as shown in Fig. 4.

In the spatially resolving mode a slit was placed at right angles to the entrance slit of the camera and close to the target. The slit width was 25 μm and the distances were chosen to give a 20× magnification. Calculations of the temporal resolution of the camera based on streak velocity, spatial resolution of the streak tube and intensifier, entrance slit width, and photoelectron energy spread from the photocathode showed that the resolution should be better than 15 psec. The sensitivity of the camera was such that a single photoelectron produced at the photocathode provided a resolvable spot on Kodak 2475 film, which is directly coupled to the fiber-optic output faceplate of the image intensifier. And indeed a weak shot produced a streak which consisted of many uniformly sized dots, each corresponding to a single channel in the microchannel plate image intensifier.

A typical spatially integrated x-ray streak is shown in Fig. 5 and its microdensitometer plot in Fig. 6. This streak shows the characteristic signature of an exploding-pusher-type experiment. The x-ray emission consists of two bursts. The
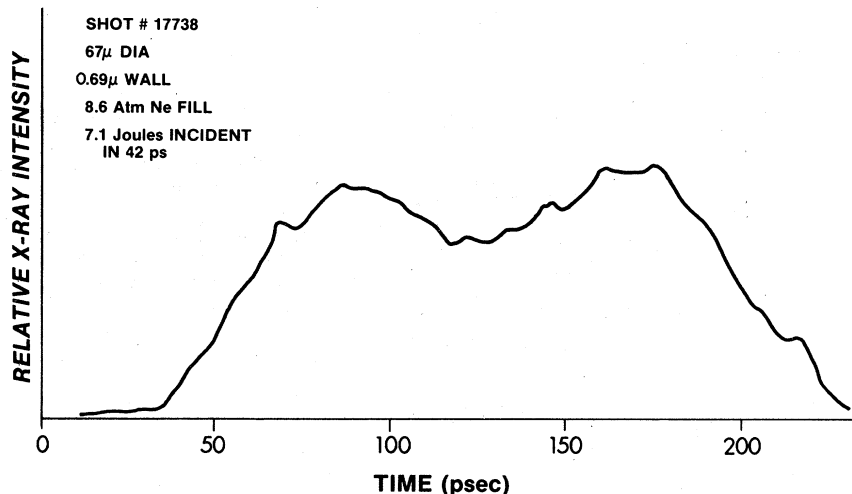

SHOT # 17738
67μ DIA
0.69μ WALL
8.6 Atm Ne FILL
7.1 Joules INCIDENT IN 42 ps

FIG. 6. Microdensitometer trace of streak in Fig. 5.
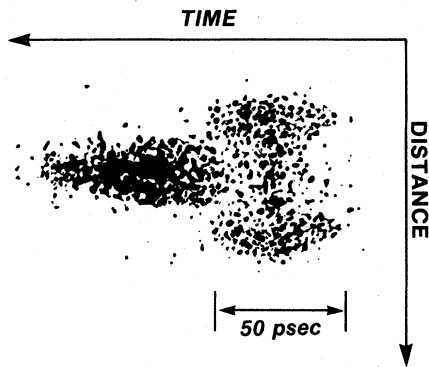
TIME

FIG. 7. Time and space resolved x-ray emission of implosion from shot No. 17639.

40 psec after the peak of the laser pulse due to continued coronal heating. Also, peak compression happens a comparable time after the second peak, since the radiation and conduction losses cool the core while compression is still taking place. The implosion velocity calculated with the LILAC code for the implosion of Fig. 6 is 2×10^7 cm sec. This is consistent with the x-ray streak camera results and is also of the magnitude necessary to explain the asymmetry of the Ly_α line of neon by Doppler effects (see below).

Figure 7 shows an example of the streaked one-dimensional x-ray image of the target. This clearly shows that the second peak comes from a central region inside the original shell.

III. X-RAY SPECTROSCOPY OF NEON

A. Principles of the method

Compression diagnostic methods employed here are based on spectral as well as spatial profiles of x-ray emission of neon lines. In addition, the electron temperature in the compressed gas can be deduced from intensity ratios of various neon lines and also from intensity ratios of such lines and the continuum. We show in Fig. 8 examples of the spectra obtained from neon-filled microballoons at two fill pressures and use them to illustrate the principles of the analysis. Spectra like these were obtained consistently and

first one rises in intensity as the incident laser pulse turns on and then later decreases in intensity as the shell coasts inward, and the incident pulse begins to decrease. Then when the shell slows down and stagnates against the compressed fill, a second burst of x rays is emitted. Detailed calculations with the hydrodynamic code show that these signals cannot be directly interpreted as explosion time and peak compression time, respectively. The first x-ray peak occurs up to
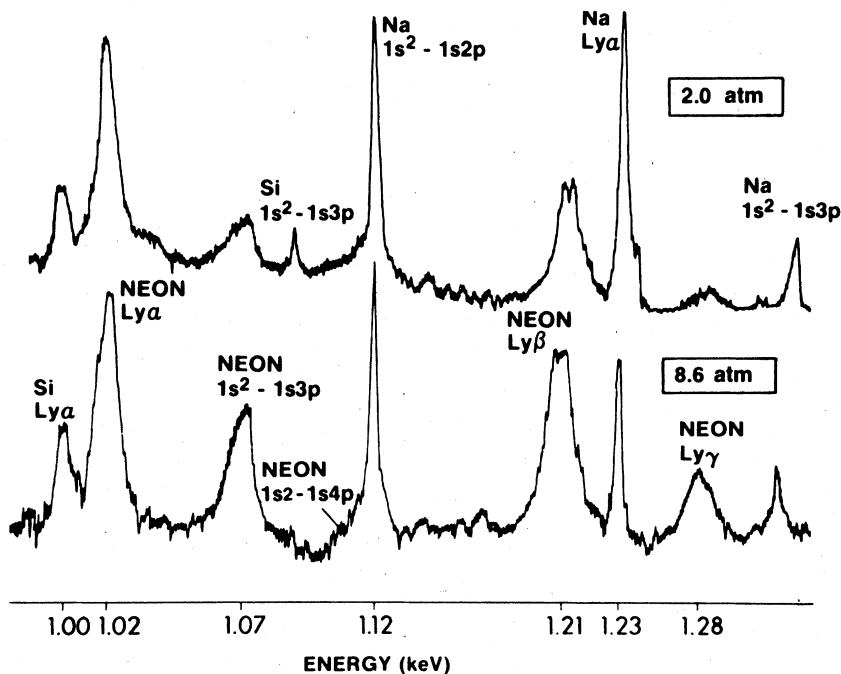

FIG. 8. Microdensitometer traces of the x-ray spectrum (in the same scale) at two different fill pressures. Sodium and silicon lines (in second order) come from the glass shell. Note the wider lines of neon.

quite reproducibly on single-shot exposures. Note the good line to background contrast ratio; this enabled us to study in detail line profiles and line-to-continuum ratios. Neon lines of the hydrogenlike ion (Ne^{9+}) and the heliumlike ion (Ne^{8+}) appear in this energy range. As the figure shows, neon lines are much broader than the sodium and silicon lines (from the glass shell). Their width ranges from 6 to 16 eV, whereas the instrumental width (due to crystal imperfections and source size as discussed in Sec. II) is about 1.5 eV. This means that the lines are broadened by physical processes in the target itself. Two such processes can cause these large widths: Stark broadening[10] and opacity broadening,[11] since at these temperatures Doppler broadening is negligible. Of course, opacity merely broadens lines which are already broadened by a primary mechanism, such as Stark effects. The first process is the result of the electric microfields in a dense plasma, and the second is the result of self-absorption (i.e., reabsorption by neon ions) causing saturation and therefore flattening of the central portion of the line profile. Stark broadening depends mainly on the plasma density (and weakly on the temperature) and pacity broadening depends on the product ρR (or more precisely on the integral $\int_0^R \rho \, dr$), where the mass density ρ is integrated over the radius of the compressed core. Actually, only the ions having the spectral transition under discussion can absorb the line, and hence the line broadening yields the product $\rho(Ne^{Z+})R$ for a transition in the Ne^{Z+} ionic species. We then need an atomic model to relate this parameter to the total ρR. However, over a wide temperature range of interest the fraction $\rho(Ne^{9+})/\rho$ will be shown to vary little with the temperature. As is well known, the ρR parameter (equivalent to $n\tau$ in magnetic confinement facilities) is important to measure since it determines the nuclear yield at a given temperature and also determines the threshold for α-particle reabsorption (or "nuclear burn").

Figure 8 compares the spectra obtained from 2.0- and 8.6-atm-fill pressure cases and indicates the degree of saturation (i.e., self-absorption) of various lines. Comparing the intensity of neon lines relative to the sodium lines as we go from the low-pressure to the high-pressure case, the Lyman-α line is unchanged, Lyman-β nearly doubles, and Lyman-γ and the heliumlike neon lines increase by a factor of 3–4. We can readily understand this behavior as follows: as the ρR of an emitting source is increased (for a given temperature) the intensity of a spectral line first increases, but when the optical depth τ_0 at the line center is about 1 the line saturates at the

blackbody limit, given by the Planck function for the pertinent temperature. Further increases in ρR only broaden the line. Figure 8 indicates that for the 8.6-atm case, the Lyman-β line intensity approaches the saturation limit (roughly the same as the Lyman-α line) and therefore has for this case a peak optical depth $\tau_0 \sim 1$ and a somewhat lower value for the 2.0-atm case. Lyman α for both cases has $\tau_0 \gg 1$ and Lyman γ has $\tau_0 \lesssim 1$, thereby increasing in intensity in proportion to the ratio of fill pressures. This is a very fortunate situation because the two extreme cases exist in the same spectrum: Lyman α is dominated by opacity broadening and yields the value of ρR, whereas Lyman γ is dominated by the Stark effect and yields the density ρ. If higher ρR values are realized in future experiments, we may then reproduce this situation by reducing the amount of neon in the target. At still higher compressions neon lines would broaden to the point of being of little use for diagnostics; however, a higher-Z dopant may then become appropriate.

These assertions about the optical depth in the Lyman series are shown later to be consistent with the ρR values derived from the lines. As we proceed to higher members of the Lyman series, the Stark width increases (roughly as $n^2 - 1$, where n is the quantum number of the upper level). The optical depth decreases both because the line broadens and because the line oscillator strength f decreases. This explains why the optical depth in Fig. 8 was found to decrease sharply in going from the Ly_α line to Ly_β and Ly_γ. Also, the linewidths along this series increase slower than by a factor proportional to $n^2 - 1$ (i.e., like 3, 8, and 15, respectively) indicating that Lyman α and possibly Lyman β are further broadened by opacity effects.

B. Stark profiles

Stark profiles of Ne^{9+} lines for the conditions prevailing in our experiments were calculated recently by Tighe and Hooper,[12] and also by Griem *et al.*[13] The profiles calculated by the former were actually used to fit the measured profiles. We show in Fig. 9 examples of such profiles used in our analysis. Note that Doppler and instrumental broadening were folded in. These profiles are mostly sensitive to the plasma density but also slightly to the temperature. As we show below, the temperature is determined experimentally before the appropriate choice of theoretical profiles is made.

These Stark profiles were calculated in a similar manner to earlier calculations for low-Z plasmas.[10] The broadening due to ions was
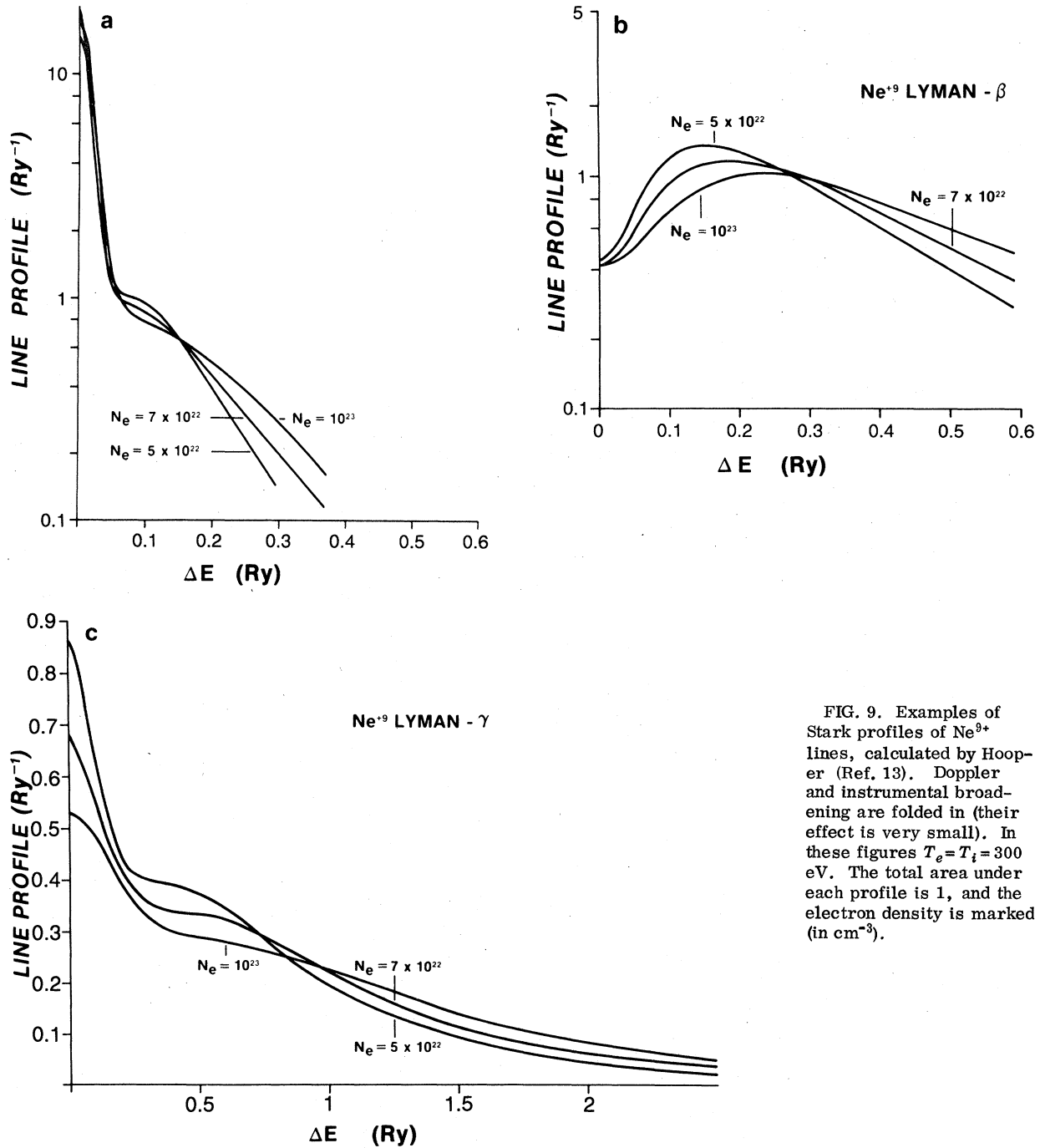
FIG. 9. Examples of Stark profiles of Ne^{9+} lines, calculated by Hooper (Ref. 13). Doppler and instrumental broadening are folded in (their effect is very small). In these figures $T_e = T_i = 300$ eV. The total area under each profile is 1, and the electron density is marked (in cm^{-3}).

treated in the quasistatic approximation, where the appropriate microfield distribution function has been previously calculated.[12] This function was compared with Monte Carlo calculations and was shown to yield about 10% precision in the ion-broadened profile for typical cases. The broaden-

ing due to electrons is subject to much larger uncertainties. In particular, excessive broadening of the central feature of the Lyman-α line in hydrogen was attributed by Griem[14] to a broadening mechanism not considered before: low-frequency electron field fluctuations. The profiles used

here[12] do not account for this effect. We in fact find below, for the Lyman-γ line of neon (see Fig. 12), indications of additional electron broadening. However, the approximations made in calculating the contribution from perturbing electrons make it preferable to reply primarily on the wings where the quasistatic theory applies to broadening by ions, and the theory of electron broadening is rather accurate. This indeed will be the case here. The overall precision of density determination is about ±20%, relying on the wings of the profile. A fuller discussion of reliability and ranges of applicability of such profiles is given by Griem *et al.*[13]

There are two types of Stark profiles for Lyman lines: the lines $1s$-np, with n even, are split into an odd number of components, and the central unshifted component appears as a spike broadened only by electrons, superimposed on a wide base broadened mainly by ions. The reason for this is that the shift due to ions of the various Stark components (which is linear in the electric field for hydrogenic ions) is larger than the second-order effect due to collisions with electrons. For lines $1s$-np, where n is odd, there is no unshifted Stark component, and the profile has a central dip. In our spectra, the Lyman-γ line appears to have a central spike, but not as sharp as predicted. The Lyman-β line has a central dip. The central spike of the Lyman-α line is missing because self-absorption has flattened that part of the profile (the spike is easily absorbed because it is very narrow), which in fact is self-reversed in many cases.

The profiles described below assume that the perturbing plasma consists entirely of Ne^{9+} ions. In reality the plasma contains mainly Ne^{8+}, Ne^{9+}, and Ne^{10+} ions. However, the differences between the profiles due to these three perturbers are small. Also, the total broadening will be very close to that due to the average charge (for example, the width for a given N_e depends on the perturber's charge only as $Z_p^{1/3}$).

C. Opacity-broadened profiles

Opacity-broadened lines are analyzed using a simplified model which assumes that the source of emitted radiation is uniform. Code calculations which do not make this assumption and which follow the temporal and spatial variations in the emitted profile of neon lines give similar results. The solution of the one-dimensional radiative-transfer equation

$$\frac{dI(\nu)}{dx} = \epsilon(\nu) - k(\nu)I(\nu) \tag{1}$$

for this case is straightforward:

$$I(\nu) = B_T(\nu)\{1 - \exp[-\tau_0 P(\nu)/P(0)]\} \tag{2}$$

Here $\epsilon(\nu)$ is the emission per unit time, volume, frequency interval, and solid angle, $I(\nu)$ is the radiation flux in the same units, $B_T(\nu)$ is the Planck blackbody radiation function, $k(\nu)$ the absorption coefficient, $P(\nu)$ the line profile, $P(0)$ the profile at line center, and τ_0 the optical depth at line center. If $\tau_0 \gg 1$ the line has a flat top, the width of which is given approximately by the condition $\tau_0 P(\nu)/P(0) = 1$. As we approach the line center from the wings we observe radiation which is integrated over smaller and smaller depths inwards from the surface. Only when $\tau_0 \ll 1$ will the observed profile $I(\nu)$ have the same shape as the local (here Stark) profile. If the temperature falls off along the edge of the emitting source, the profile $I(\nu)$ may show a dip in the center. However, the total linewidth and falling wings will be relatively insensitive to inhomogeneities (especially near the surface) since they are emitted over the whole depth of the source. Hence it is not surprising that a detailed numerical-code calculation and a crude model are found to agree quite well.

Profiles $I(\nu)$ are fitted to optically thick lines and the ratio $\tau_0/P(0)$ derived. This ratio is directly related to the product ρR through

$$\tau_0/P(0) = (\pi e^2/mMc)f\rho Rb. \tag{3}$$

Here M is the mass of the ion and f the oscillator strength of the line. Once we know the density from an optically thin line we can find $P(0)$ corresponding to the appropriate Stark profile. Finally, b is the fraction of all neon ions which are in the lower level of the absorbed transition, i.e., the ground level of Ne^{9+} ions. In order to get an estimate on b we plot in Fig. 10 results from two atomic models: local thermodynamic equilibrium[16] LTE and the corona model.[16] In the corona model we calculate the steady state of the various charge states of neon by balancing ionization through electron collisions[15] with ground-state ions and radiative recombination.[15] We only consider here three charge states (Ne^{8+}, Ne^{9+}, and Ne^{10+}) and plot $b = n(Ne^{9+})/[n(Ne^{8+}) + n(Ne^{9+}) + n(Ne^{10+})]$ as a function of temperature. The condition for the first excited state not to be in collisional (LTE) equilibrium with the ground state is[16]

$$N_e < 3 \times 10^{18} Z^6 T^{1/2}, \tag{4}$$

where T is in keV. For our case this means $N_e \lesssim 10^{24}$ cm,[3] which is shown below to be the case. However, opacity (self-absorption) of the resonance line may move the system away from
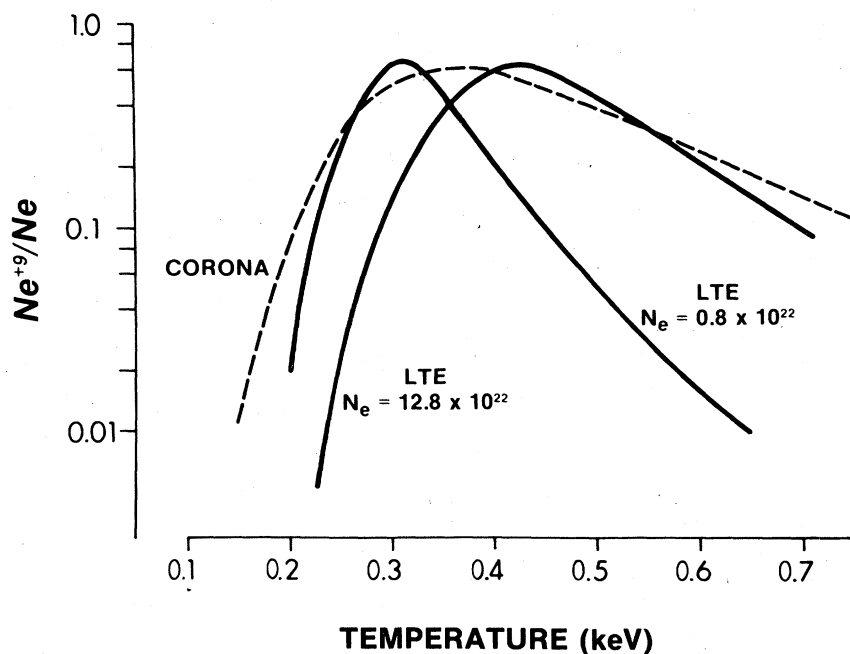
FIG. 10. Fraction of neon ions which are in the Ne^{9+} charge state, calculated in local thermodynamic equilibrium (LTE) at two electron density values (in cm^{-3}) and in corona equilibrium (which is density independent).

corona equilibrium and closer to LTE. We therefore also plot in Fig. 10 results from a complete LTE model. Unlike the case for the corona model, the parameter b in LTE depends on the density in addition to its dependence on the temperature. The density values in Fig. 10 were chosen to be below and above the values obtained in these experiments. Even though the curves differ they all have comparable peak values. This means that in any of these cases with the exception of the high-pressure 55.6-atm case, b will have about the same value when most of the line intensity is emitted, even though this will occur at a different temperature and therefore a different time in each case. An average value of b according to any of these curves, provided the maximum temperature during the compression is at least 250–300 eV, is 0.3. This value is in good agreement with the much more detailed code calculations. In the high-pressure case, we will overestimate b using this value, and hence the inferred ρR will be a lower bound. An improved estimate of the temperature is not possible due to the strong line reversal.

D. Analysis of measured neon line profiles

We now apply the methods described above to a few characteristic spectra obtained from neon-filled microballoons.

Before applying these methods to measured line profiles we need an estimate of the electron
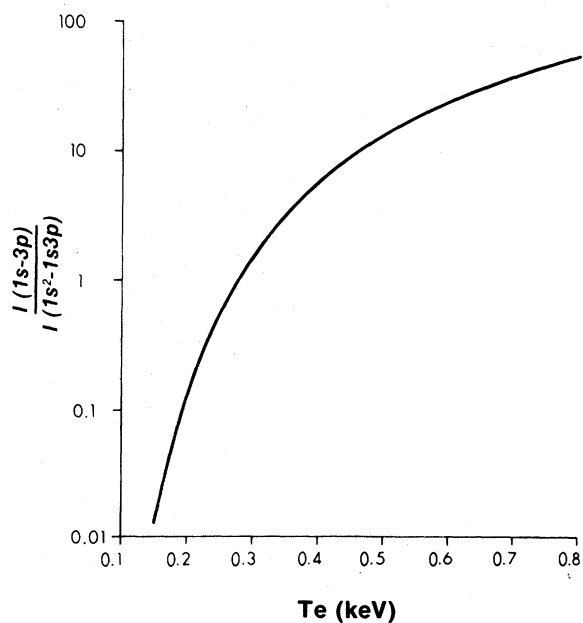

FIG. 11. Intensity ratio of the lines $1s\text{-}3p$ of Ne^{9+} and $1s^2\text{-}1s\,3p$ of Ne^{8+}.
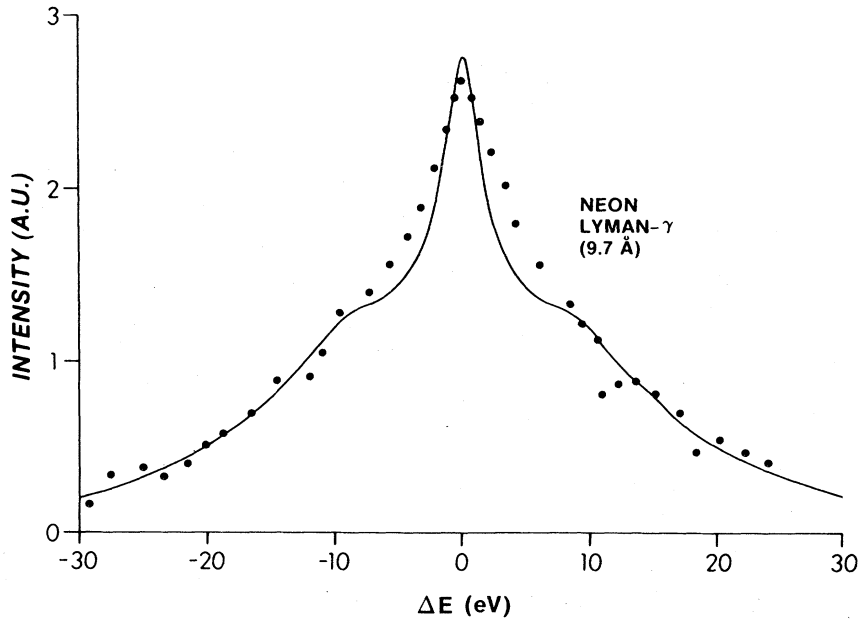
FIG. 12. Fitting a Stark profile (which includes Doppler and instrumental broadening) to the experimental profile of the Lyman-γ line of Ne^{9+} (at 9.7 Å). The profile corresponds to an electron density $N_e = 7 \times 10^{22}$ cm^{-3} and $T_e = T_i = 300$ eV. The intensity is measured in arbitrary units (A.U.).

temperature T_e. A first estimate can be obtained using the 8.6-atm case (Fig. 8), where both Ly_α and Ly_β lines were shown to be optically thick. This means that their peak intensities should lie approximately on the same Planckian distribution corresponding to an effective surface temperature. Their intensity ratio is then given by

$$R = I(Ly_\alpha)/I(Ly_\beta)$$

$$= (E_1/E_2)^\alpha (e^{E_2/kT} - 1)/(e^{E_1/kT} - 1) , \qquad (5)$$

where E_1, and E_2 are the energies of the Ly_α and Ly_β transitions. The quantity α lies between 3 and 5 and depends on the spectrometer dispersion which in turn depends on geometry. Since.

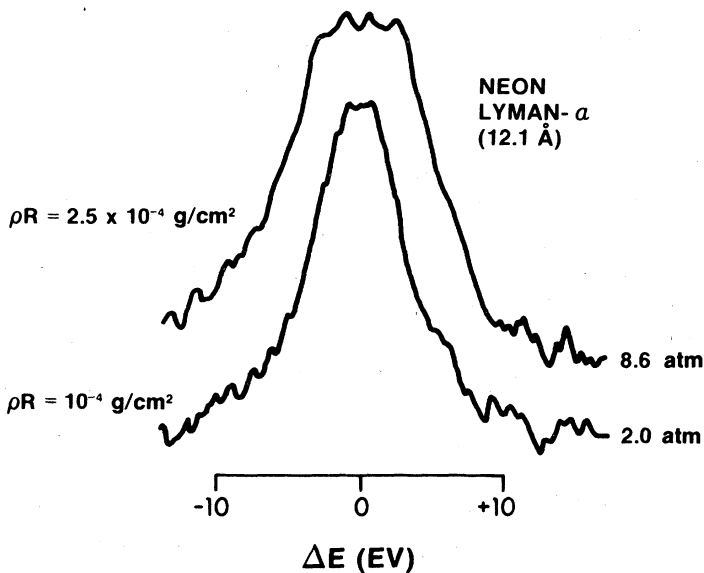## ρR MEASUREMENT: OPACITY-BROADENED PROFILES OF THE X-RAY LYMAN-a LINE OF NEON

FIG. 13. Measured profiles of the Lyman-a line of Ne^{9+} (12.134 Å) at two different neon fill pressures of the target.
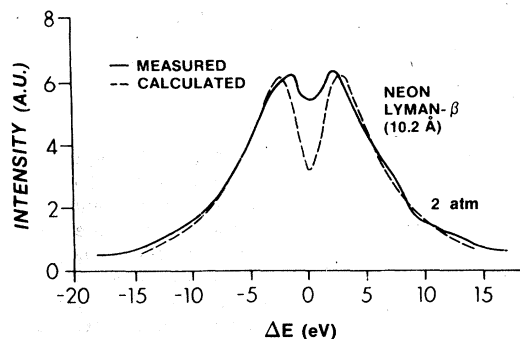
FIG. 14. Fitting of a Stark profile (which includes Doppler and instrumental broadening) to the measured profile of the Lyman-β line of Ne^{9+} (10.239 Å), at 2.0-atm neon-fill pressure. The theoretical profile corresponds to $N_e = 7 \times 10^{22}$ cm^{-3}, $T_e = T_i = 300$ eV. The intensity is measured in arbitrary units (A.U.).

$E_1/E_2 \sim 1$ we find $T \simeq 270$ eV for $R = 1.2$.

An additional temperature estimate is obtained by calculating the integrated intensity ratio $R_3 = I(1s-3p)/I(1s^2-1s3p)$. These lines (especially for the 2-atm case) are relatively free of self-absorption, which simplifies the modeling. By definition, the intensity ratio R_3 can be related to the population densities in the upper levels
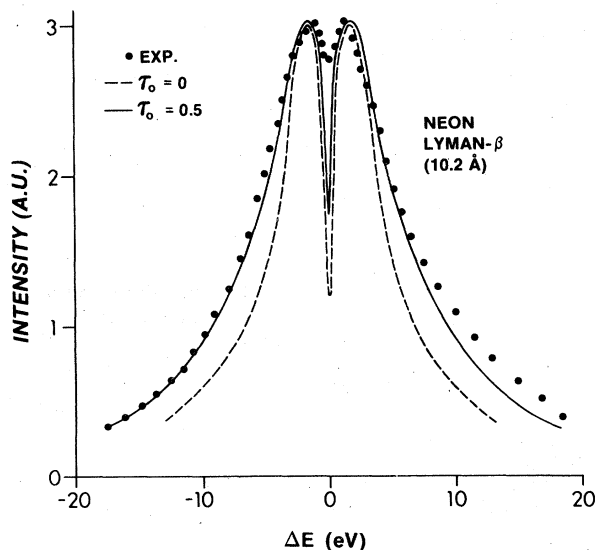

FIG. 15. Same as Fig. 14, for a fill pressure of 8.6-atm neon. τ_0 is the assumed optical depth at the line center. The intensity is measured in arbitrary units (A.U.).

through $R_3 = A_{1-3}^H (h\nu)^H n_3^H / A_{1-3}^{He} (h\nu)^{He} n_3^{He}$, where H refers to the hydrogenlike and He to the helium-like species. Inserting the Einstein emission probabilities we get $R_3 = 0.25 n_3^H / n_3^{He}$. These populations can be related via the Saha equation to the densities in the ground levels of the next-higher ionization state. The condition for this to be valid is approximately[17] $N_e > 5 \times 10^{21} \sqrt{T}$, where T is in keV. For $T = 0.3$ keV the condition is $N_e > 2.7 \times 10^{21}$ cm^{-3}, which will be shown below to be valid. We obtain then

$$R_3' = 3 (n_1^{+10}/n_1^{+9})(e^{-0.151/T})/(e^{-0.122/T}), \qquad (6)$$

where again T is in keV. The ground-state population ratio can be computed in the so-called corona approximation (see above) which means that it is given by the ratio of the ionization coefficient and the radiative recombination coefficient. Figure 11 is the final plot of R_3. The spectra in Fig. 8 show an intensity ratio of about $R_3 \sim 1.5$, which corresponds in Fig. 11 to $T \sim 300$ eV. We note that a factor-of-2 error in R_3 will only result in a 13% error in T. Numerical modeling of the implosion will be shown below to yield a very similar value of temperature.

Knowing the temperature enables us to choose the correct Stark profiles for interpreting the results if we assume that the ion temperature equals the electron temperature. In the case of DT-filled microballoons, the ion temperature can be considerably higher than that of the electron temperature. However, for higher-Z fills such as neon, the electron-ion partition times are significantly shorter resulting in similar electron and ion temperatures.

We now fit Stark profiles corresponding to $T_e = T_i = 300$ eV to some typical experimental profiles at 2- and 8.6-atm fill pressures. Figure 12 shows a best-fit profile for the Lyman-γ line (9.7 Å). Here and below, Doppler and instrumental broadening effects are folded into the Stark profile but they have a negligible effect. The theoretical profile corresponds to an electron density 7×10^{22} cm^{-3}, which is equivalent to a mass density of about 0.25 g/cm^3. The uncertainty in N_e due to uncertainties in the temperature and the assumed background level was estimated to be ±25%. Note that the (electron-broadened) central spike is broader than predicted by the theory we used. This is related to the uncertainties in computing the electron contribution as discussed above. Assuming now that the whole neon mass was uniformly compressed, we derive a diameter $D = 19$ μm for the compressed neon core and a ρR value of 2.5×10^{-4} g/cm^2 (here R is the average chord length $2D/\pi$). The resulting compression ratio is 38. For the 2.0-atm case the final density is

(a)

Si
LYMAN-α

(b)

Ne^{+3}
LYMAN-α
(Theoretical)

INSTRUMENTAL
WIDTH   1.2eV

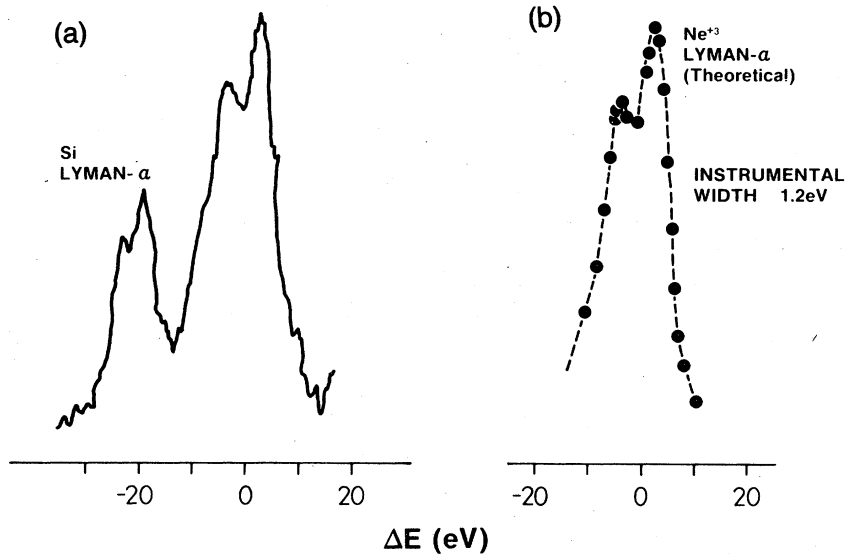-20   0   20   -20   0   20

ΔE (eV)

FIG. 16. Asymmetric and
self-reversed Lyman-α
line of Ne^{9+}. (a) Measured
profile from an 8.6-atm
neon fill pressure micro-
balloon. (b) Computed
profile from Eq. (11) with
$\tau_0 = 86$ and $\Delta\lambda = 2.37$ mÅ;
instrumental broadening
has been folded in.

approximately the same and the compression
ratio is about 150.

Moving now to the opacity-broadened Lyman-α
line we show in Fig. 13 measured profiles for the
2.0- and 8.6-atm cases. The lines have a flat top
which is predicted for a spatially uniform source.
Fitting the profile emanating from a uniform ab-
sorbing source [Eq. (2)] to the measured profile
at 8.6 atm we obtain $\tau_0/P(0) = 2 \times 10^{16}$ sec^{-1}, using
the Lyman-α Stark profile for $N_e = 7 \times 10^{22}$ cm^{-3}.

From Eq. (3) we get $\rho R = 2.2 \times 10^{-4}$ g/cm^2, in good
agreement with the value obtained above. The
optical depth at the peak of the unshifted Stark
component is ~86. For the 2.0-atm case ρR ~
1×10^{-4} g/cm^2.

We finally fit Stark profiles to the Lyman-β line,
which is an intermediate case between the heavily
absorbed Lyman-α and the nonabsorbed Lyman-γ
line. The best fit for the 2.0-atm case (Fig. 14)
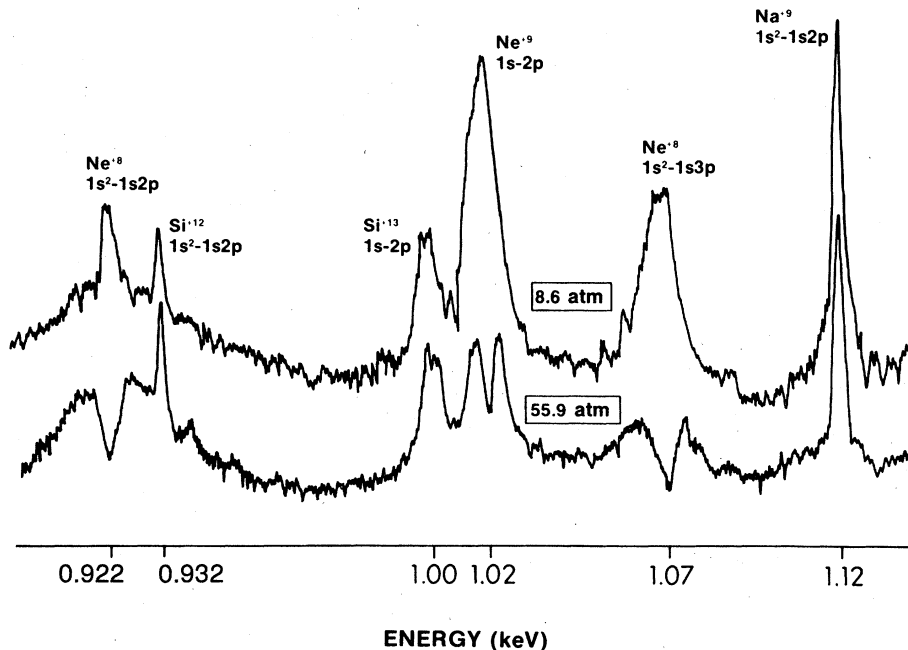is the Stark profile corresponding to $N_e = 7 \times 10^{22}$

Na^{-9}
1s^2-1s2p

Ne^{-9}
1s-2p

Ne^{-8}
1s^2-1s2p

Si^{-12}
1s^2-1s2p

Si^{-13}
1s-2p

Ne^{-8}
1s^2-1s3p

8.6 atm

55.9 atm

FIG. 17. Comparison
between the spectrum ob-
tained at two neon-fill
pressures: 8.6 and 55.9
atm. Note the self-re-
versal of neon lines.

0.922   0.932   1.00 1.02   1.07   1.12

ENERGY (keV)

cm^{-3}, the same density which was used for the Lyman-γ line. We see that both Lyman β and Lyman γ for this low-fill-pressure case can be assumed optically thin, and they lead to the same density. For the 8.6-atm case (Fig. 15) the same profile has the wrong width and shape. However, we get a good fit if we assume the profile to go through an absorption region of optical depth $\tau_0 = 0.5$ at the line center. In other words, we replace the Stark profile $P(\nu)$ by Eq. (2). The optical depth at the two peaks of the profile is 1.2, which agrees with the estimate $\tau(Ly\beta)\sim 1$ given above. It should be noted that the observed central dip is never as deep as predicted. This is a usual occurence even with Stark profiles of atomic hydrogen and is attributed to both theoretical uncertainties near the line center and experimental uncertainties such as source inhomogeneities and insufficient resolution.

We can check whether the estimates on the optical depth of the three Lyman lines given above are consistent with the results found here. The optical depth can be found from Eq. (3). At line center for Lyman β, P_λ for $N_e = 7 \times 10^{22}$ cm^{-3} is 3.55×10^8 cm^{-1}. For the ρR values obtained above and again assuming that one third of the neon ions are in the Ne^{9+} state we get for the line center $\tau_0(Ly_\beta) = 0.7$, in excellent agreement with Fig. 15. For the 2-atm case we get $\tau_0(Ly_\beta) \sim 0.35$. The optical depth for Ly_α and L_γ also follow from Eq. (3). For the 8.6-atm case we find $\tau_0(Ly_\alpha) = 110$, $\tau_0(L_\gamma) = 0.71$. It should be noted that the optical depth τ_0 is about the same for Ly_β and Ly_γ. However, for Ly_β, τ first increases as we move away from line center, whereas for Ly_γ, τ decreases very rapidly.

Lines which show self-reversal (i.e., absorption which results in a dip in the center of the line profile) permit a crude determination of the inward velocity. A self-reversed line is emitted deep inside the source and is absorbed in a cooler region near the surface. A relative motion of the emitting and absorping layers will therefore result in a relative shift between the dip in the profile and the center of symmetry of the wings on both sides of the dip. This shift (too small to be determined with accuracy) causes the two profile peaks flanking the central dip to be of unequal intensity. The intensity ratio between these two peaks is the experimental parameter we use to estimate the fill-gas velocity. Figure 16(a) shows as an example the profile of the Ne^{9+} Lyman-α line at 8.6 atm. The peak of longer wavelength is the weaker of the two. We can understand this very easily: since the periphery of the compressed neon gas moves in faster than the central region, an absorbing atom sees a source
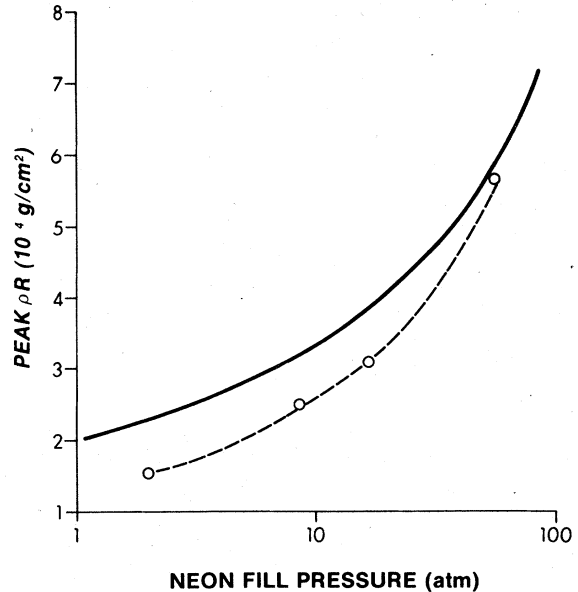

FIG. 18. Comparison of experimental and simulation results for maximum neon ρR as a function of neon-fill pressure. The circles are the experimental values deduced by the methods of Sec. III. The curves are from simulations: solid curve, maximum ρR; dotted curve, ρR at time of peak core x-ray emission.
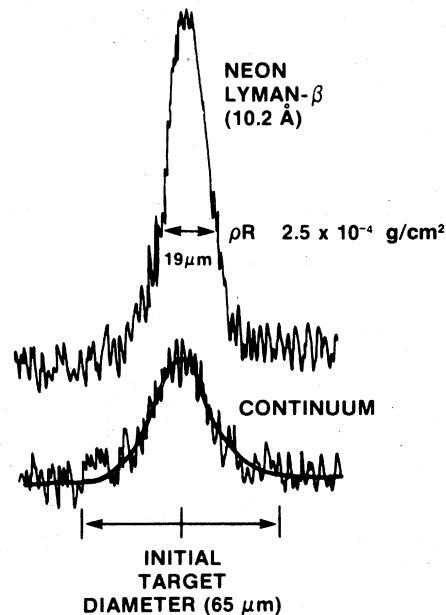

FIG. 19. Spatial profile of the Lyman-β line of Ne^{9+} (10. 239 Å), and the nearby continuum. The bar of length 19 μm indicates the diameter of the compressed neon core if we assume homogeneous compression and use the density obtained from spectral-profile analysis.

which approaches it. This atom sees then a blue-shifted profile but absorbs photons at the un-shifted (in its frame of reference) frequency, i.e., on the red side of the profile. This causes the peak of longer wavelength to be weaker. It is interesting to note that two experiments[18] with low-Z laser produced plasma have produced self-reversed lines where the peak of longer wave-length was stronger. This is to be expected be-cause in those experiments the plasma expands from a flat target rather than being compressed.

A self-reversed line profile can be approximated by the expression[19]

$$I(\lambda) = P(\lambda + \Delta\lambda) \exp[-\tau_0 P(\lambda)/P_0], \qquad (7)$$

$P(\lambda)$ being the Stark profile of the Lyman-α line and $\Delta\lambda$ the relative Doppler shift between emission and absorption layers. The profile in Eq. (7) is indeed asymmetric and self-reversed. Analysis shows that the intensity ratio between the "blue" and "red" peaks depends almost entirely on $\Delta\lambda$ and hardly on τ_0. On the other hand, the wave-length separation between the peaks depends al-most entirely on τ_0 and hardly on $\Delta\lambda$. Figure 16(b) shows the calculated profile which best fits the experimental profile, that with $\Delta\lambda = 2.37$ mÅ (and a wide range of optical depth values). Since the imploding target has a spherical geometry and only velocity components in the direction of ob-servation can cause a Doppler shift, the actual velocity difference is larger by a factor of q

than that given by the measured $\Delta\lambda$. A simple estimate of q is obtained if we assume a spherical shell moving at a velocity V into a stationary core and average $V \cos\theta$ over the half sphere facing the spectrometer (emission from the back is mostly absorbed). This results in $q = 2$. We therefore obtain for the velocity difference between the ab-sorption and emission layers

$$\Delta V = 2c\Delta\lambda/\lambda = 1.2 \times 10^7 \text{ cm/sec.} \qquad (8)$$

Since this is a differential velocity, it is somewhat lower than that predicted by the simulation when normalized to the x-ray streak camera data.

Figure 17 shows the x-ray spectrum of neon and adjacent glass lines for 55.9-atm pressure, compared with that for 8.6 atm. As can be seen, all the neon lines now appear with a prominent central dip: they are self-reversed. Theory[19] shows that self-reversal is the result of a temper-ature gradient; the relatively hot line-emitting neon plasma is surrounded by a cooler layer giving rise to the central dip.

Using the model in Eq. (2) or the one in Eq. (7) and the upper bound on the temperature as ob-tained from the central core, we estimate a lower bound on the ρR value for the 55.9-atm case to be 5.5×10^{-4} gr/cm^2. The results of ρR measure-ments as a function of fill pressure are summar-ized in Fig. 18, where comparison is made be-tween these measurements and the theoretical predictions. Predicted maximum compression is
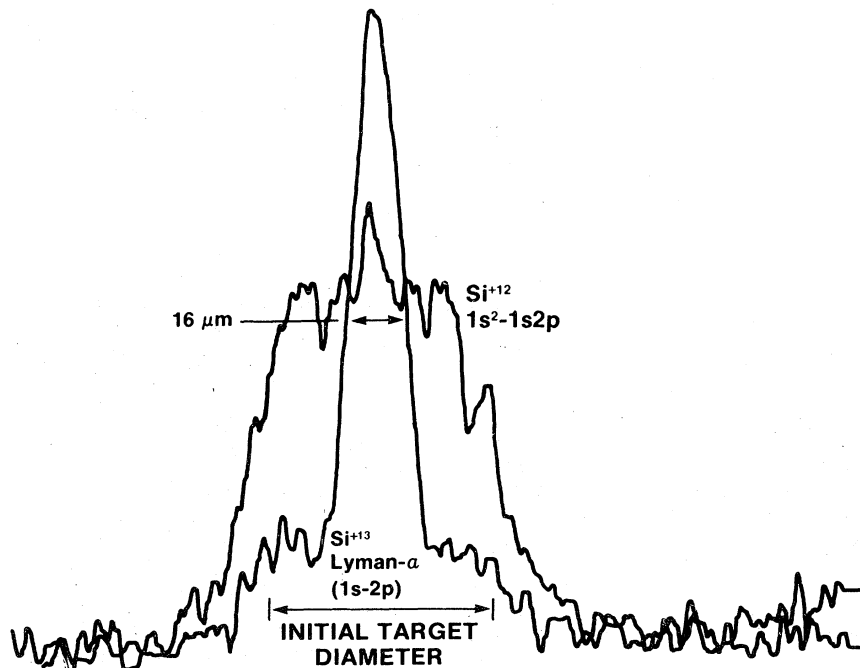

16 μm

Si^{+12} 1s^2-1s2p

Si^{+13} Lyman-a (1s-2p)

INITIAL TARGET DIAMETER

FIG. 20. Spatially re-solved Si^{13+} (1s-2p) and Si^{12+} (1s^2-1s2p) line emis-sion from laser-imploded microballoon. Note the clear presence of silicon in the core.

higher than that predicted at peak x-ray emission (or that measured) because radiation cooling causes additional compression after peak emission.

An additional important point to be retained from the high-pressure spectra is that an approach to central heating is indicated. This means that the central part of the fill gas is heated more than its periphery by the imploding glass. Central heating is an important feature of designed high-gain targets: energy is invested efficiently to only heat the core of the fuel, whereas the rest of fuel is ignited by α-particle absorption (propagating burn). One may say that at high fill pressures the implosion dynamics deviates from the explosive-pusher mode where the fill gas is heated more uniformly.

By placing a slit between the target and the spectrometer we record on film a one-dimensional image of the target as a function of x-ray wavelength. The slit width and position give a resolution of 13 μm and magnification 4. In Fig. 19 we show a scan of the target image at the wavelength of the Lyman-β line of neon (10.2 Å) and at a wavelength slightly off that line. In both cases the microdensitometer slit width was chosen to span the same wavelength band $\Delta\lambda$, approximately equal to the line full width at half maximum (FWHM). As seen, part of the emission at 10.2 Å is continuum, and it has to be subtracted to find the net emission of the line. When we do this we find the neon emission profile to have a FWHM of about 17 μm and a base width of about 29 μm. For the initial diameter of 65μm these correspond to a compression ratio of 56 and 11, respectively. These values flank the value 38 obtained from spectral profiles of neon lines. However, it is not clear whether one should use the base width or any other width, and the cubic power of the width results in a large uncertainty in the compression. These problems apply equally to compression estimates based on pinhole images of x rays or α particles. Furthermore, we only sometimes find agreement between compression values obtained from line profiles and compression values obtained from spatially resolved images such as in Fig. 19 or pinhole images. More specifically, as we go to higher fill pressures the imaging methods tend to yield incorrectly high compression values, presumably because of the central heating.

Additional information of the implosion dynamics can be obtained by comparing spatial profile of neon lines (Fig. 19) with those of silicon lines (Fig. 20). Silicon lines are emitted in the peripheral annular zone where the laser is absorbed (roughly at the original location of the glass shell). In addition, strong radiation is emitted in the center of the target where the compressed glass stagnates. The spectral profiles of silicon lines in the center shows considerable broadening (FWHM of about 10 eV) due to Stark and possibly also opacity mechanisms. The presence of silicon in the center may indicate fill-glass mixing due possibly to hydrodynamic instability or nonsphericity of the implosion. Better spatial resolution (which requires high intensity) would be needed to verify this possibility.

*On assignment from Exxon Research and Engineering Co., Linden, N.J.
†Present address: Chalk River Nuclear Laboratory, Chalk River, Ontario, KOJ1JO Canada.
‡Permanent address: 33-B Arayadai, Tokai-Mura Nakagun, Ibaraki, Japan 319-11.
§Permanent address: Exxon Research and Engineering Co., Linden, N.J.
[1]B. Yaakobi, D. Steel, E. Thorsos, A. Hauer, and B. Perry, Phys. Rev. Lett. 39, 1526 (1977); B. Yaakobi, D. Steel et al., Laboratory for Laser Energetics Report No. 74, 1978 (unpublished).
[2]J. Auerbach et al., Lawrence Livermore Laboratory, Report No. UCRL-79636, 1977 (unpublished).
[3]S. L. Bogolyubskii et al., JETP Lett. 24, 182 (1976).
[4]V. W. Slivinsky et al., Appl. Phys. Lett. 30, 555 (1977); N. M. Ceglio and L. W. Coleman, Phys. Rev. Lett. 39,

20 (1977).
[5]Extensive theoretical and experimental work on the explosive-pusher mode has been reported. See, for example, H. G. Ahlstrom, Lawrence Livermore Laboratory Report No. UCRL-79819, 1977 (unpublished); Damon Giovanielli, Los Alamos Scientific Laboratory Report No. LA-7218-MS, 1978 (unpublished); P. M. Campbell et al., KMSF Report No. U491, 1975 (unpublished).
[6]J. Delettrez and E. B. Goldman, Laboratory for Laser Energetics Report No. 36, 1976 (unpublished); LILAC replaces an earlier one-dimensional hydrodynamic code, SUPER (E. B. Goldman, Laboratory for Laser Energetics Report No. 16, 1973) (unpublished).
[7]E. K. Storm et al., Lawrence Livermore Laboratory Report No. UCRL-79788, 1977 (unpublished); M. D. Rosen and J. H. Nuckolls, Lawrence Livermore Labo-

ratory Report No. UCRL-80164, 1977 (unpublished).

[8]B. Henke and M. A. Tester, *Advances in X-ray Analysis* (Plenum, New York, 1975), Vol. 18, p. 76.

[9]R. F. Benjamin, P. B. Lyons, and R. H. Day, Appl. Opt. 16, 393, Feb. 1977.

[10]H. R. Griem, *Spectral Line Broadening by Plasmas* (Academic, New York, 1974).

[11]See, for example, *Plasma Diagnostics*, edited by W. Lochte-Holtgreven (North-Holland, Amsterdam, 1968), Chaps. 1 and 4.

[12]R. J. Tighe and C. F. Hooper, Phys. Rev. A 15, 1773 (1973); 17, 410 (1978); C. F. Hooper (private communication).

[13]H. R. Griem, M. Blaha, and P. C. Kepple, Phys. Rev.

A (to be published).

[14]K. Grutzmacher and B. Wende, Phys. Rev. A 16, 243 (1977); H. R. Griem, *ibid.* 17, 214 (1978).

[15]See, e.g., W. Lotz, Astrophys. J. Suppl. 14, 207 (1967); M. J. Kunze *et al.*, Phys. Rev. 165, 267 (1968); M. J. Seaton, Mon. Not. R. Astron. Soc. 119, 81 (1959).

[16]H. R. Griem, *Plasma Spectroscopy* (McGraw-Hill, New York, 1964), pp. 151 and 159.

[17]Reference 16, p. 148.

[18]G. Tondello, E. Jannitt, and A. M. Malvezzi, Phys. Rev. A 16, 1705 (1977); F. E. Irons, R. W. P. McWhirter, and N. J. Peacock, J. Phys. B 5, 1975 (1972).

[19]R. D. Cowan and G. H. Dicke, Rev. Mod. Phys. 20, 418 (1948).
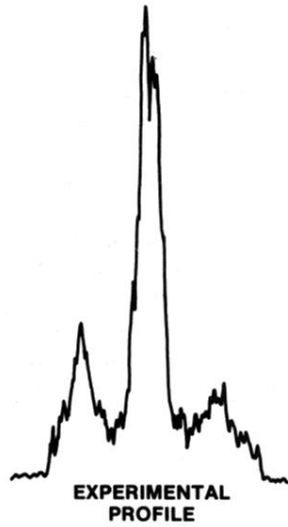
70 μm
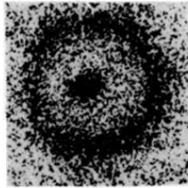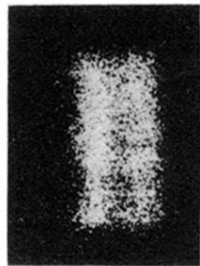
EXPERIMENTAL
PROFILE

FIG. 2. Typical x-ray pin-
hole exposure and densito-
meter trace of a neon-filled
target.

TIME → ⊢—⊣
      30 psec

FIG. 5. Time resolved
x-ray emission of implo-
sion from shot No. 17738.